

Finite Element Study of the Stress Field Near Pressurized and Non-Pressurized Flaws in Rock Specimens Subject to Uniaxial and Biaxial Loads

Gunarathna, G.S.

New Jersey Institute of Technology, Newark NJ, United States of America

Gonçalves da Silva, B.

New Jersey Institute of Technology, Newark NJ, United States of America

Copyright 2018 ARMA, American Rock Mechanics Association

This paper was prepared for presentation at the 52nd US Rock Mechanics / Geomechanics Symposium held in Seattle, Washington, USA, 17–20 June 2018. This paper was selected for presentation at the symposium by an ARMA Technical Program Committee based on a technical and critical review of the paper by a minimum of two technical reviewers. The material, as presented, does not necessarily reflect any position of ARMA, its officers, or members. Electronic reproduction, distribution, or storage of any part of this paper for commercial purposes without the written consent of ARMA is prohibited. Permission to reproduce in print is restricted to an abstract of not more than 200 words; illustrations may not be copied. The abstract must contain conspicuous acknowledgement of where and by whom the paper was presented.

ABSTRACT: The finite element code ABAQUS is used to model a typical granite specimen subjected to either uniaxial or biaxial compression, with two pre-fabricated flaws with the geometry 2a-30-30 in which only one flaw is pressurized. The maximum and minimum principal stresses as well as the maximum shear stresses are analyzed around the flaw tips and along the bridge between the inner flaw tips of the pressurized and non-pressurized flaws. When the specimen is loaded uniaxially, the maximum principal stresses in the bridge between inner flaw tips are tensile near the pressurized flaw and decrease significantly as one moves towards the non-pressurized flaw. For the biaxial loading, mainly compressive principal stresses are observed for low hydraulic pressures; tensile stresses start to develop for larger hydraulic pressures, but only near the pressurized flaw. For both uniaxial and biaxial cases, tensile and shear cracks may occur near the pressurized flaw but are not theoretically possible near the non-pressurized flaw.

1. INTRODUCTION

Hydraulic fracturing is becoming a common process used in the exploitation of oil and gas entrapped within shale formations as well as in the mining of heat in Enhanced Geothermal Systems and in Artificial Groundwater Recharge. While there are a number of studies on the initiation and propagation of hydraulic fractures under uniaxial loading, limited experimental and numerical studies focus on the effect of biaxial loads on the stress field around pressurized and non-pressurized fractures. As extensively discussed by previous studies, one of the major concerns involved with the hydraulic fracturing applications is the path at which new crack propagate. Bobet (1997) used molded gypsum specimens with either open or closed pre-fabricated flaws under uniaxial and biaxial loading conditions to observe the crack initiation, propagation and ultimate coalescence of the specimens. Bobet (1997) described several significant observations, the most important of which are shown in table 1, as they are relevant to the present study.

Most authors, such as Lajtai (1971), Wong (2008) and Yang et al. (2008) have tested Plaster-of-Paris, Carrara marble and molded gypsum under uniaxial, biaxial and triaxial conditions. Other researchers have experimentally propagated fractures using a hydraulic pressure inside pre-fabricated flaws, while simultaneously visualizing the

entire fracturing process. In fact, Gonçalves da Silva (2016) used granite specimens subjected to different vertical loads while increasing the hydraulic pressure inside two flaws and AlDajani (2017) tested prismatic shale specimens with pre-fabricated flaw(s) and observed the interaction between induced hydraulic fractures with a pressurized and a non-pressurized flaws.

Despite these experimental efforts, many researchers have been conducting numerical simulations to better predict the fracturing behavior due to both mechanical and geometrical complexities involved in the testing procedures. Since rock masses usually have discontinuities in the form of cracks, fractures and joints, it is important to incorporate these discontinuities in the numerical analyses. With the recent computational advances, a number of numerical studies have been conducted on crack initiation and propagation criteria based on stress and strain fields as well as on energy dissipation around the tips of the cracks introduced into the rock matrix. Currently, a number of numerical techniques are typically used to evaluate the crack initiation and propagation, such as the Finite Element Method (Rice, 1968; Carpinteri, 1991), Boundary Element Method (Chan, 1986; Vasarhelyi & Bobet, 2000) and Displacement Discontinuity Method (Gordeliy & Detournay, 2011; Liu, 2016).

Table 1. Observations of study conducted by Bobet (1997) on pre-cracked gypsum specimens under uniaxial and biaxial loading conditions

Observation	Uniaxial Loading	Biaxial Loading
Wing Cracks	<ul style="list-style-type: none"> Initiate from the flaw tips. Large wing cracks. 	<ul style="list-style-type: none"> Small wing cracks, which initiate from the middle of the flaw for $\sigma_h \leq 5.0$ MPa. No wing cracks for $\sigma_h > 5.0$ MPa.
Secondary Cracks	<ul style="list-style-type: none"> Initiate at the same stress as wing cracks. 	<ul style="list-style-type: none"> Initiate before the wing cracks.
Coalescence	<ul style="list-style-type: none"> Coalescence stress increases with the flaw angle, ligament length and confining stress. Closed flaws have higher coalescence stresses than open flaws. 	
Failure	<ul style="list-style-type: none"> Coincides with coalescence 	<ul style="list-style-type: none"> After coalescence

Additionally, other methods are being used to simulate the fracturing of rock, such as the hybridized displacement discontinuity and indirect boundary element method (Chan et al., 1990), Discrete Element Method (Potyondy & Cundall, 2004), and the Extended Finite Element Method (Yu, 2011). It should be noted that each technique has its own merits and weaknesses, whose description is not in the scope of this paper. While much effort has been dedicated to experimentally and numerically understand the initiation and propagation of cracks under different loading conditions, there has not been many thorough studies focusing on the combined effect of uniaxial or biaxial loading and hydraulic pressure inside pre-fabricated flaws. This paper investigates the variation of the stress field around two pre-fabricated flaws when only one is hydraulically pressurized and the specimen is subjected to either uniaxial or biaxial loading conditions. This loading condition will be experimentally assessed by the authors of this paper in research currently being conducted.

This paper first discusses the methodology used in the numerical analyses and the different loading cases considered under uniaxial and biaxial loading conditions. Then, the findings are discussed and subsequently a conclusion is presented. It should be noted that, throughout this paper, the term ‘flaw’ is used to refer to a pre-fabricated fracture while the term ‘crack’ is used to denote a newly-formed fracture.

2. METHODOLOGY

The finite element code ABAQUS is used to model a typical granite specimen with two pre-fabricated flaws with the geometry $2a-30-30$ ($L-\beta-\alpha$) and under either uniaxial ($\sigma_v \neq 0$ and $\sigma_h = 0$) or biaxial ($\sigma_v \neq 0$ and $\sigma_h \neq 0$) loading conditions as illustrated in figure 1. The model used in the ABAQUS is considered to be linearly elastic. Therefore, all the results obtained are valid before any cracks initiate. The material properties assigned in the model are as follows, based on the Barre granite tested by Miller (2008).

- Young’s modulus - 19.2 GPa
- Poisson’s Ratio - 0.25

The aperture of the flaws is taken as 0.7mm with semi-circular tips, as obtained for the waterjet-cut flaws in prismatic granite specimens. The boundary conditions used for the uniaxial and biaxial loadings are shown in figure 2.

Figure 2a shows the boundary conditions for the model with uniaxial loading in which the nodes of the elements in the bottom horizontal boundary were restrained to move in both vertical and horizontal directions. The elements in the vertical edges were kept free to move in both directions. Figure 2b shows the boundary conditions for the biaxial loading: the lower horizontal boundary is restrained to move in the vertical direction and one vertical boundary was restrained to move in the horizontal direction.

The finite element mesh used for the analyses is shown in figure 3. The mesh was made finer near the flaws compared to the boundaries, since it is near the flaws and flaw tips where the stress concentrations will occur.

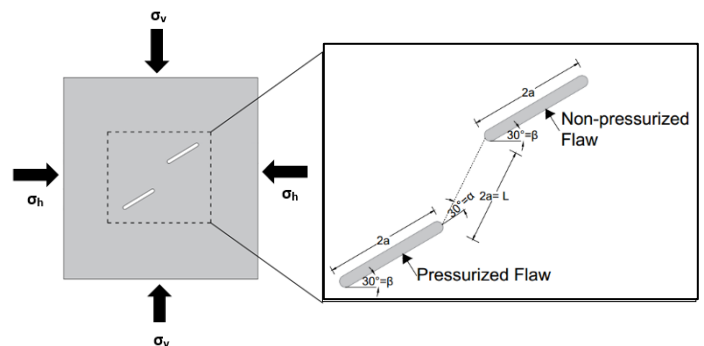


Fig. 1. Studied double-flaw geometry ($L-\beta-\alpha$) and loading conditions.

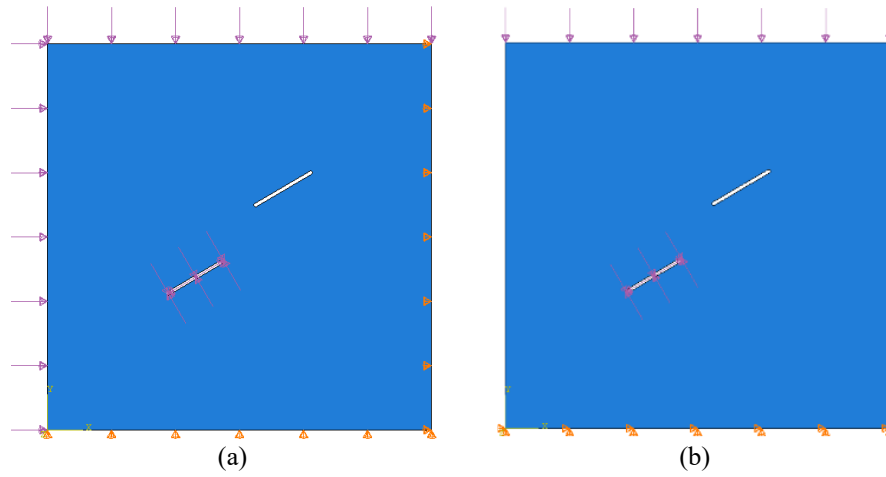


Fig. 2. Boundary conditions considered for (a) uniaxial loading and (b) biaxial loading in the model.

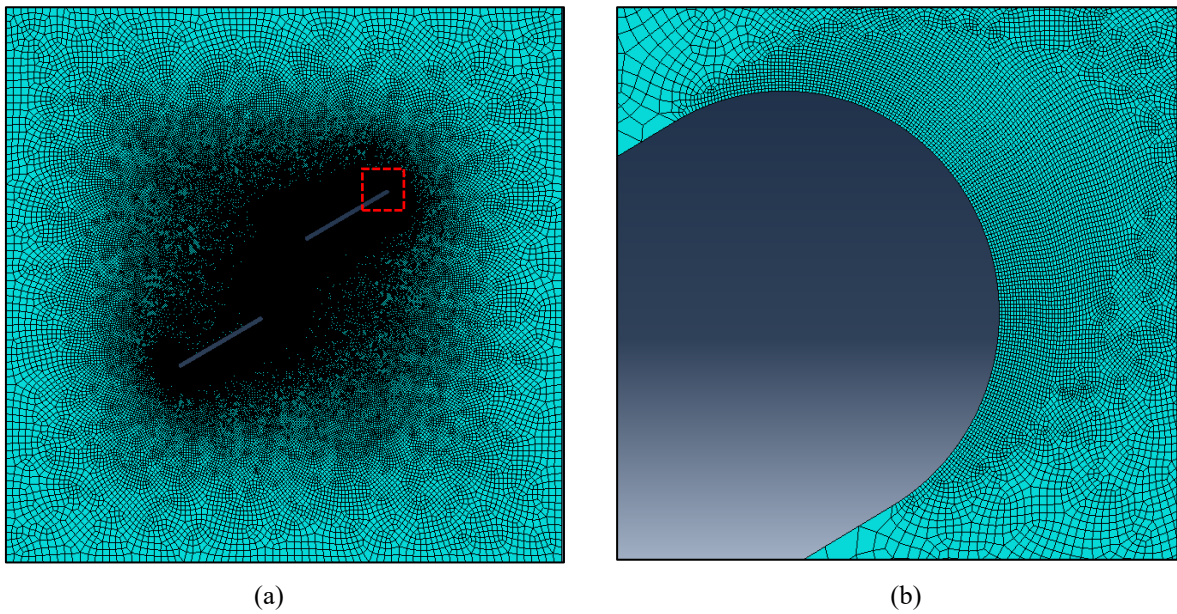


Fig. 3. a) Finite element mesh used for the analyses (b) Detail of the mesh near the tips.

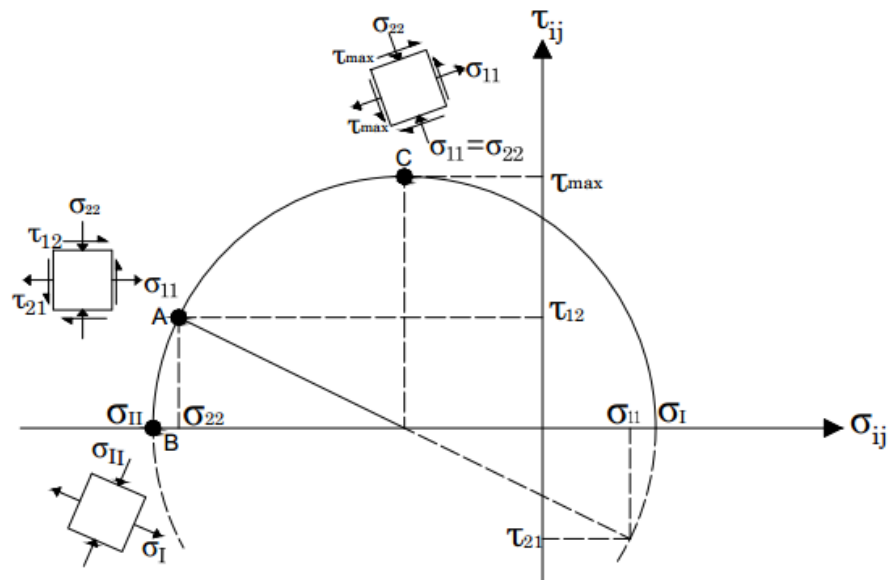


Fig. 4. Mohr circle showing the maximum and minimum principal stresses (σ_I and σ_{II}) and maximum shear stress (τ_{max}) for certain elements (Gonçalves da Silva & Einstein, 2014).

A quadrilateral linear plane stress element mesh is used in the analyses. These elements were used since the displacements are more accurately interpolated than with triangular elements.

2.1. Analyzed Stresses

In order to analyze the stress field around the flaws, it is important to first understand the directions of maximum principal stresses and maximum shear stresses. Gonçalves da Silva & Einstein (2014) graphically illustrated the different normal and shear stress combinations for elements with various orientations using the Mohr circle (figure 4). Element A is oriented along the vertical and horizontal axes and hence subjected to generic normal and shear stresses. Element B is only subjected to principal stresses (σ_I and σ_{II}) hence no shear stresses are acting on it. Element C is oriented in the direction of maximum shear stress and, consequently, normal stresses are similar in both directions. As earlier mentioned, the linear elastic model used in this study allows one to study the initiation of cracks but is not applicable to their propagation. Therefore, in order to evaluate the stress fields obtained and relate them to possible crack initiation, it is considered that tensile cracks may initiate from the locations where the maximum tensile principal stresses (σ_I in Element B) are the highest and shear cracks may initiate from the locations where the maximum shear stresses (τ_{max} in Element C) are the highest.

It is important to point out that the sign convention used in ABAQUS and adopted in the current paper considers

tensile stresses to be positive and compressive stresses to be negative.

2.2. Loading Cases and Paths Considered in the Analysis

As explained previously, the analyses were conducted for both uniaxial and biaxial loading conditions. Tables 2 and 3 describe the different loading cases considered for the uniaxial and biaxial loadings, respectively.

Table 2. Uniaxial loading conditions analyzed

Load Case	Vertical Load (VL) (MPa)	Hydraulic Pressure (HP) in Pressurized Flaw (MPa)	Hydraulic Pressure in Non-pressurized Flaw (MPa)
0	10	0	0
1	10	2.5	0
2	10	5	0
3	10	10	0
4	10	20	0
5	10	40	0

Table 3. Biaxial loading conditions analyzed

Load Case	Vertical Load (VL) (MPa)	Horizontal Load (HL) (MPa)	Hydraulic Pressure in Pressurized Flaw (MPa)	Hydraulic Pressure in Non-pressurized Flaw (MPa)
0	10	10	0	0
1	10	10	2.5	0
2	10	10	5	0
3	10	10	10	0
4	10	10	20	0
5	10	10	40	0

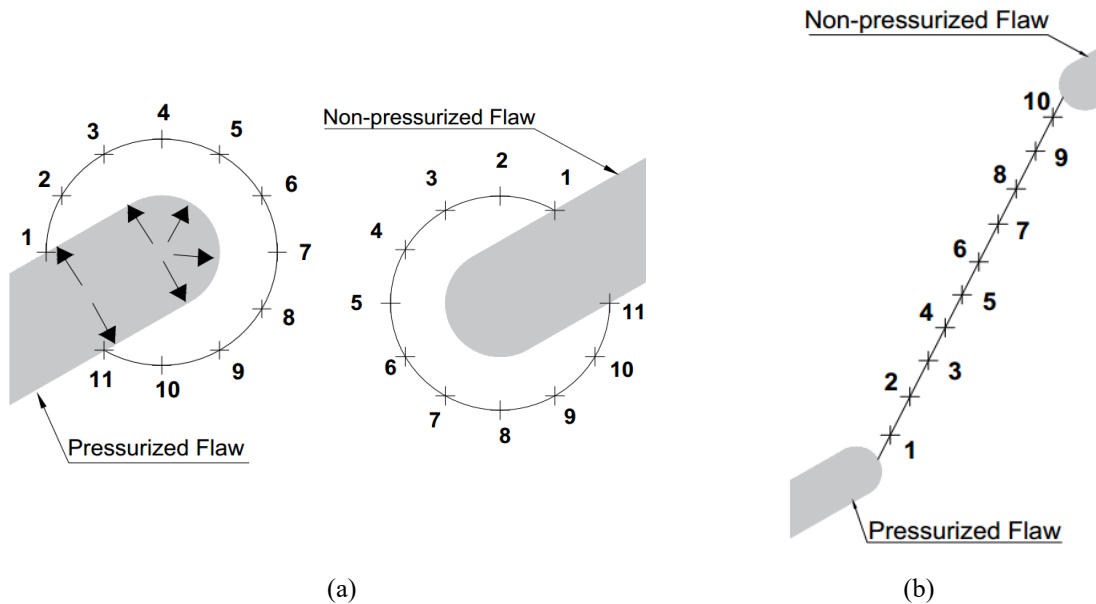


Fig. 5. Paths along which stresses were analyzed (a) Circular path around the flaw tips (b) Along the bridge region between the pressurized and non-pressurized flaws.

For the uniaxial loading conditions, a vertical load of 10 MPa is simultaneously applied with a hydraulic pressure in only one flaw, which was varied from 2.5 MPa to 40 MPa (table 2). Similarly, for the biaxial loading condition, both vertical and horizontal loads were applied and a hydraulic pressure, which was also raised from 2.5 MPa to 40 MPa, was applied in one of the flaws (table 3). The vertical and horizontal loads were considered similar (10 MPa). In order to systematically evaluate the variation of the stress field, these regions were investigated:

- In a large region including both flaws;
- Around the flaw tips along a circular path with twice the radius of the semi-circular flaw tip (figure 5a);
- Along the bridge region connecting the inner tips of the pressurized and the non-pressurized flaws (figure 5b).

3. RESULTS

3.1. Stresses in the Region of Flaws

In this section of the paper, the variation of the maximum principal stresses (σ_1) is analyzed. First, the uniaxial loading cases shown in table 2 are discussed in Subsection 3.1.1 followed by the biaxial loading cases shown in table 3 in Subsection 3.1.2.

3.1.1 Uniaxial Loading Condition

Figure 6 shows the maximum principal stress contours for Case 0 under uniaxial loading. High tensile stresses are observed near the tips of both flaws and identified by circles (The tips of the right flaw is enlarged to show the exact locations of highest tensile maximum principal stresses). Hence, tensile cracks can initiate from these locations. The highest compressive maximum principal stresses are located ahead of both flaw tips.

Figure 7 (a to e) shows the variation of the maximum principal stresses as the Hydraulic Pressure (HP) is increased from 2.5 MPa to 40 MPa in the pressurized flaw. Increasingly high tensile maximum principal stresses are observed near both flaw tips only for load Case 1 (figure 7a). For load Cases 2 to 5 the highest tensile maximum principal stresses are observed only near the tips of the pressurized flaw, as intuitively expected. Hence, tensile cracks can be expected to initiate from the tips of the pressurized flaw as HP is increased from 2.5 MPa to 40 MPa. As observed previously, the highest compressive maximum principal stresses are located ahead of both flaw tips for Case 0. However, as HP is increased in the pressurized flaw, it is observed that the compressive stresses move towards the long edges of the pressurized flaw. On the other hand, for the non-pressurized flaw, compressive maximum principal stresses are still observed ahead of the both tips as HP is increased from 0 to 40 MPa.

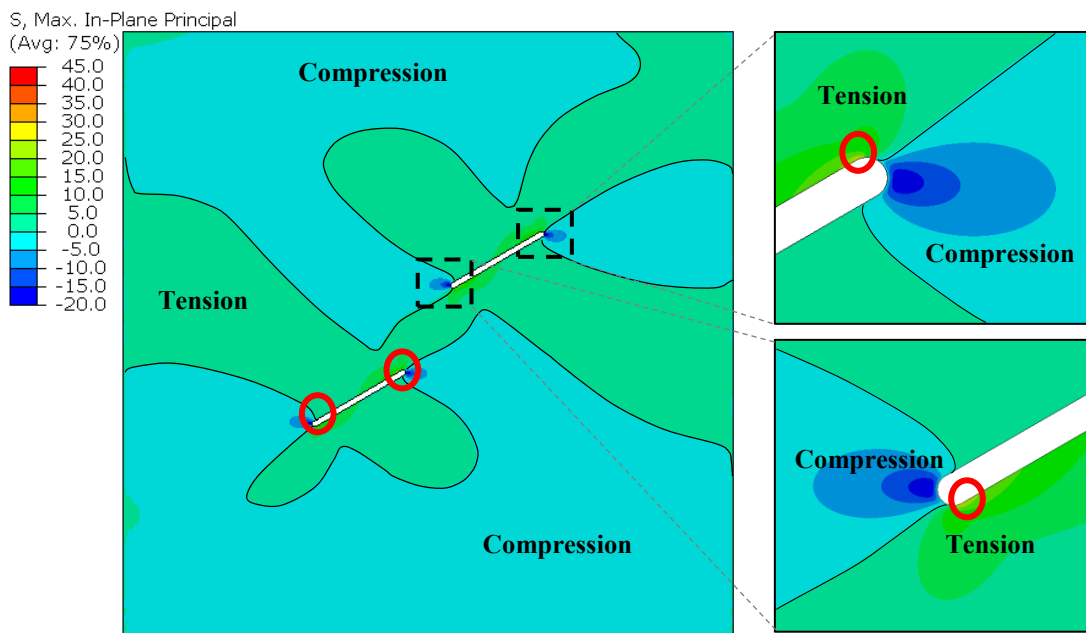
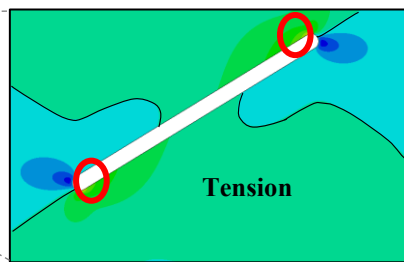
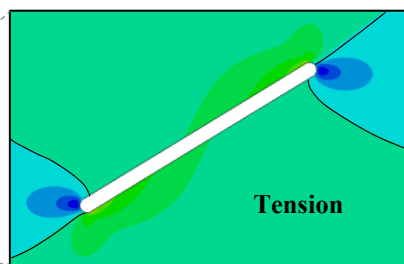
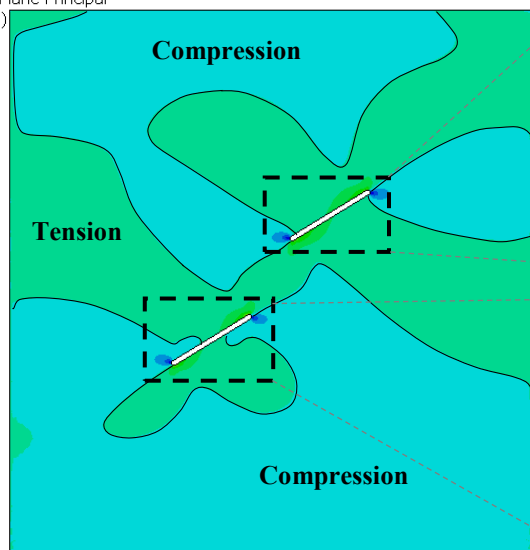
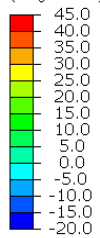


Fig. 6. Maximum principal stress contours for Case 0 under uniaxial loading with circles showing the location of the highest tensile stress.

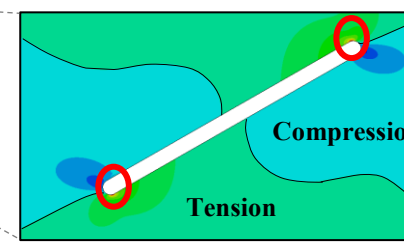
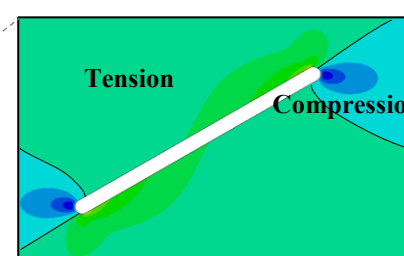
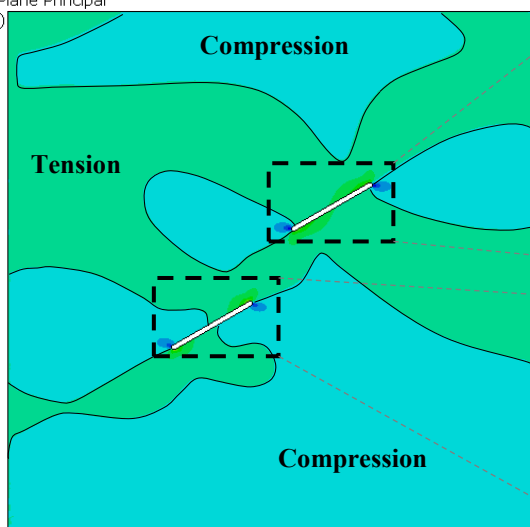
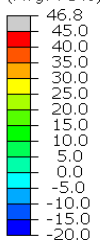
Note: The same color scale was used in figures 6 and 7 to facilitate the interpretation of the variations of the stresses.

S, Max. In-Plane Principal
(Avg: 75%)



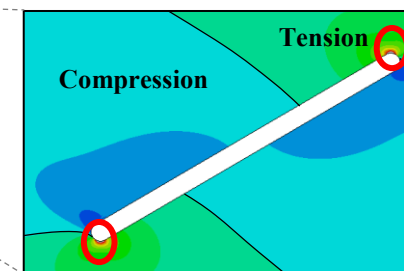
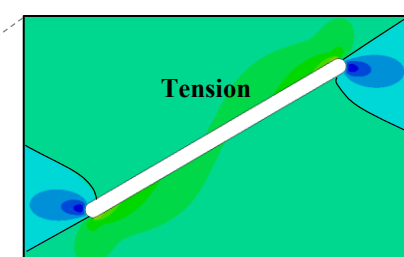
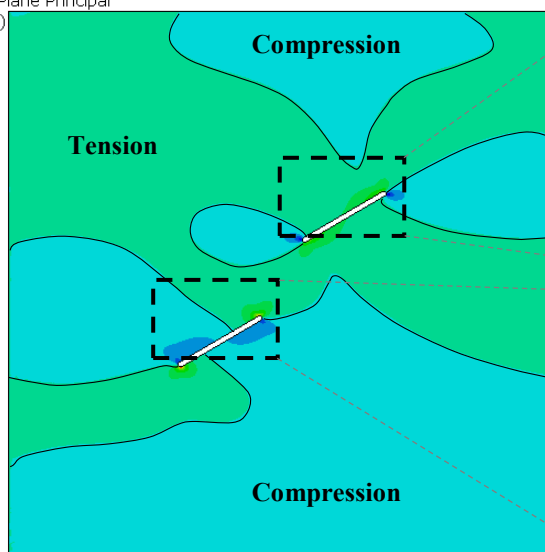
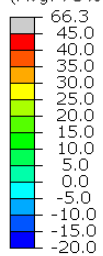
(a)

S, Max. In-Plane Principal
(Avg: 75%)

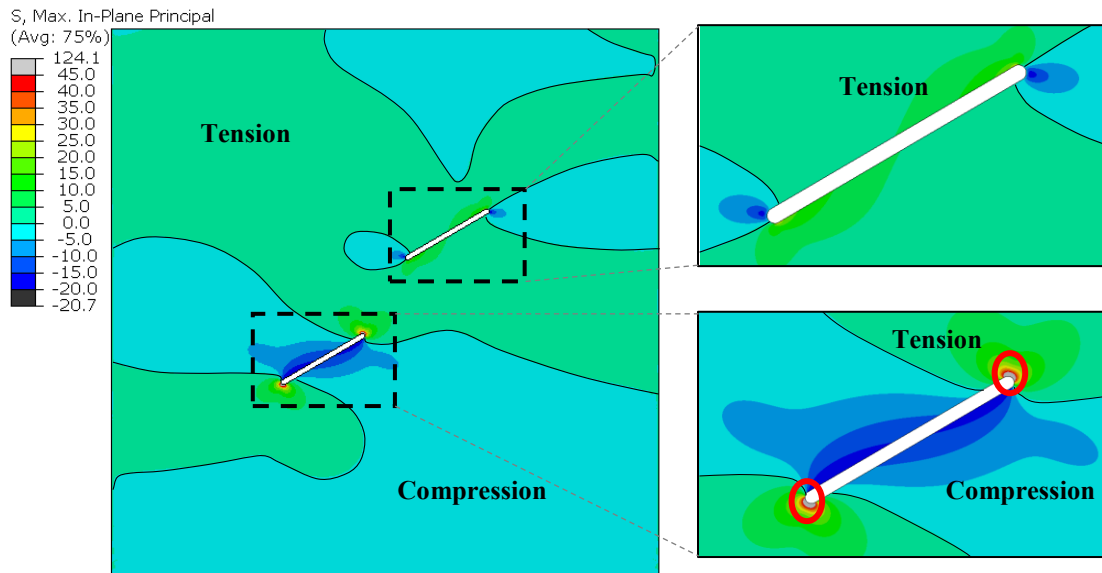


(b)

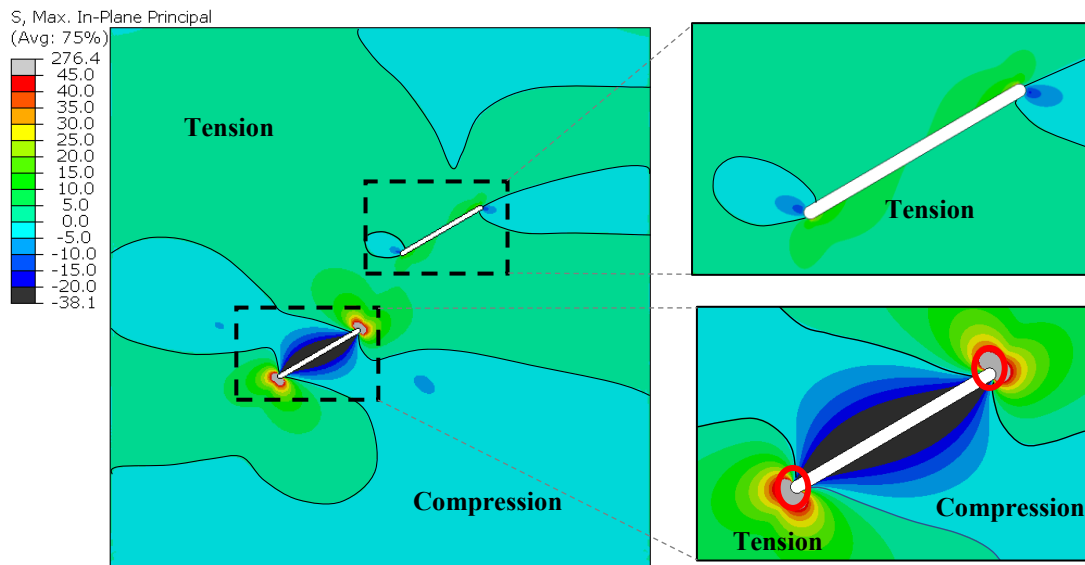
S, Max. In-Plane Principal
(Avg: 75%)



(c)



(d)



(e)

Fig. 7. Maximum principal stress contours under uniaxial loading with circles showing the location of the highest tensile stress (a) Case 1 (b) Case 2 (c) Case 3 (d) Case 4 (e) Case 5.

Note: The same color scale was used in figures 6 and 7 to facilitate the interpretation of the variations of the stresses.

3.1.2 Biaxial Loading Condition

Figure 8 shows the maximum principal stress contours for Case 0 under biaxial loading. There is a significant difference in magnitude of tensile stresses compared to figure 6 for Case 0 under uniaxial loading. The circles show the location of the highest tensile maximum principal stress. It is noticeable that the magnitude and area under tension are significantly smaller than under uniaxial compression. Figure 9 (a to e) show the variation of the maximum principal stress as HP is increased from 2.5 MPa to 40 MPa in the pressurized flaw.

When HP increases from 2.5 MPa to 10 MPa (figure 9 a to c), it is noted that the area around the pressurized flaw is completely in compression while the non-pressurized flaw is slightly in tension. However, when HP is larger than 10 MPa (figure 9 c to e), both tips of the pressurized flaw become highly tensile whereas the non-pressurized flaw tips are always in compression. Based on the analysis, tensile cracks may initiate from the tips of the pressurized flaw, but only when HP is larger than 10 MPa.

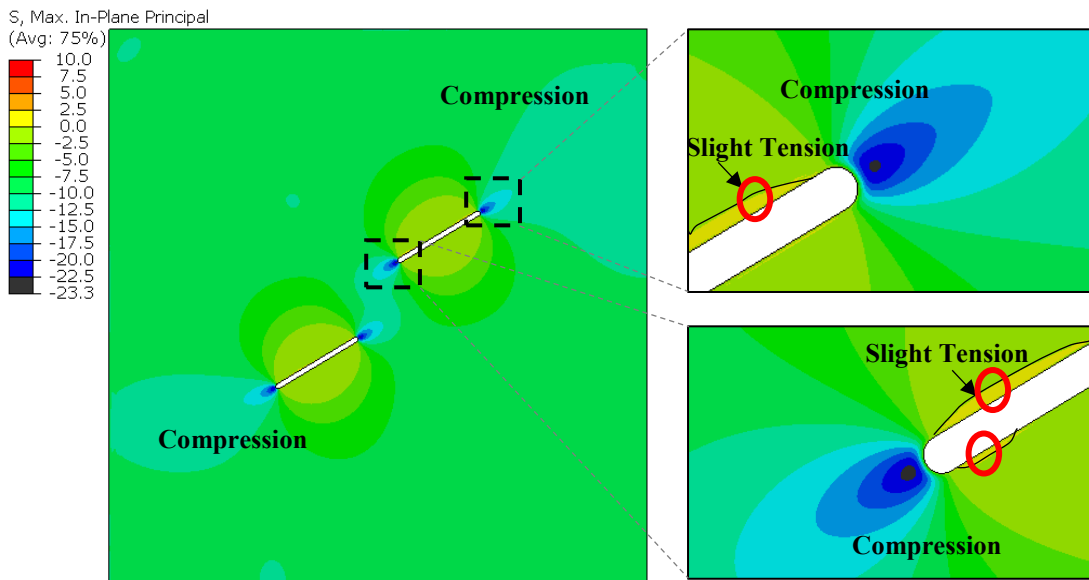
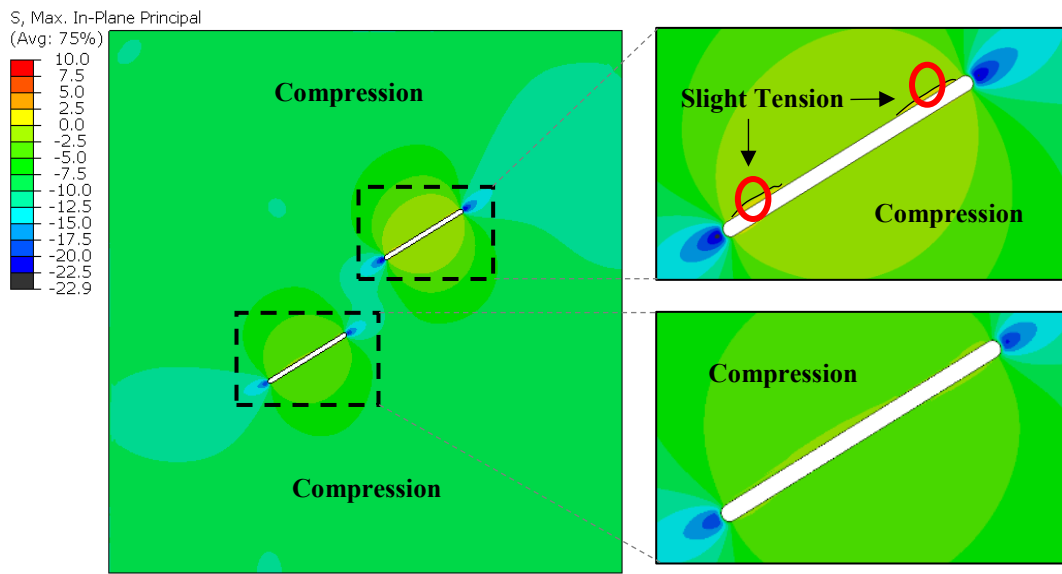
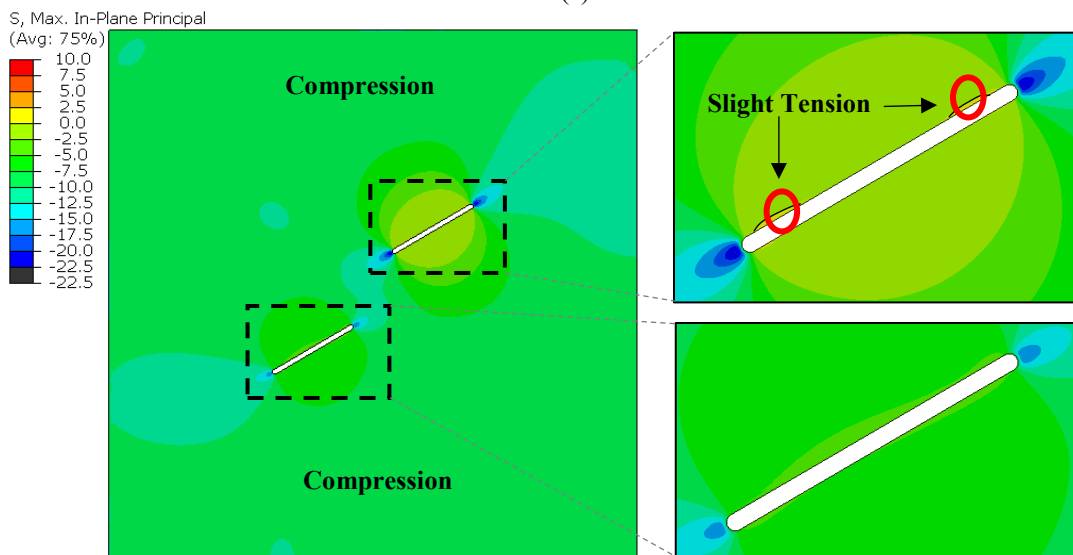


Fig. 8. Maximum principal stress contours for Case 0 under biaxial loading with circles showing the location of the highest tensile stress.

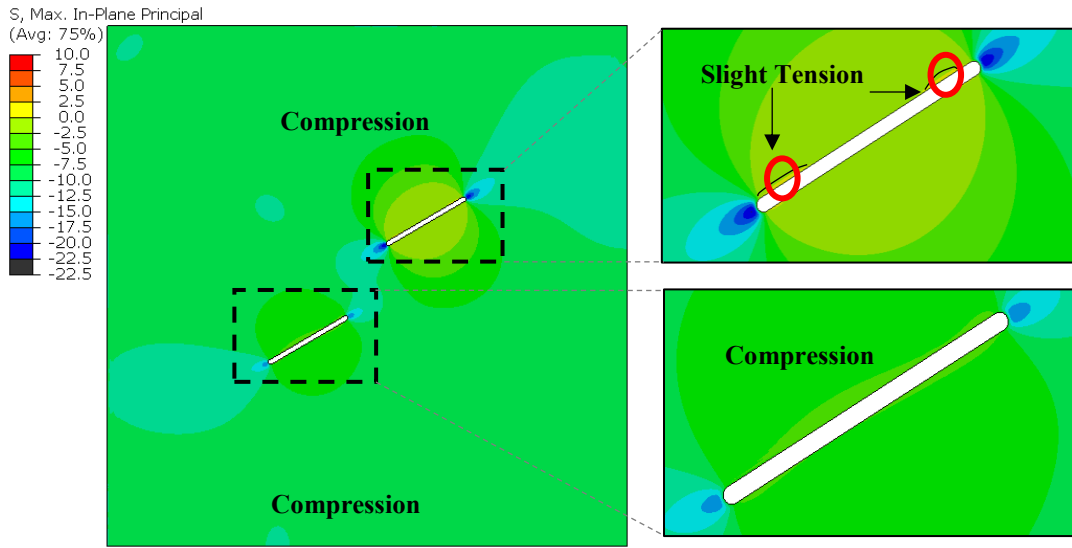
Note: The same color scale was used in figures 8 and 9 to facilitate the interpretation of the variations of the stresses.



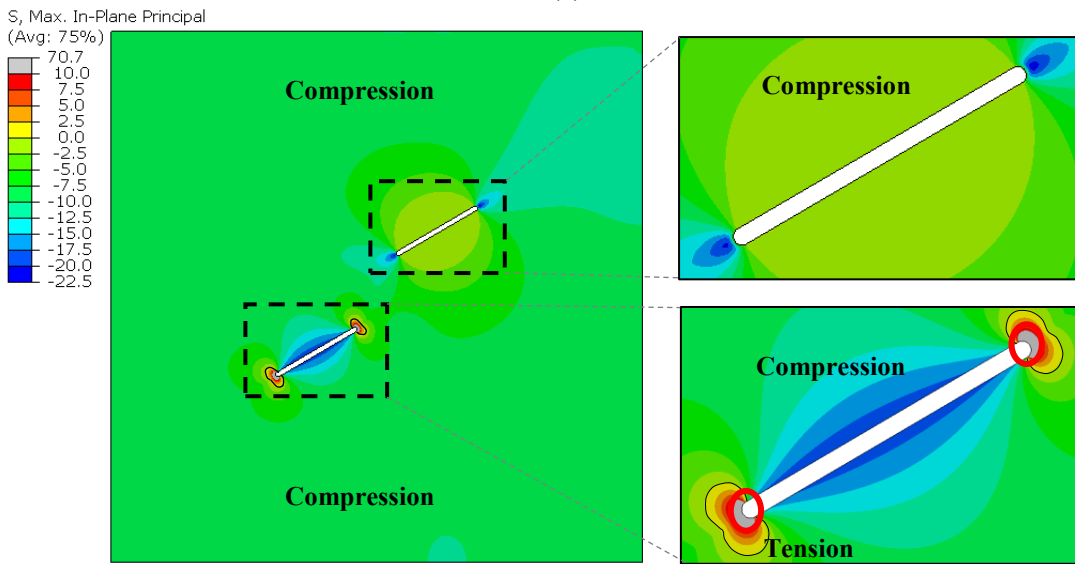
(a)



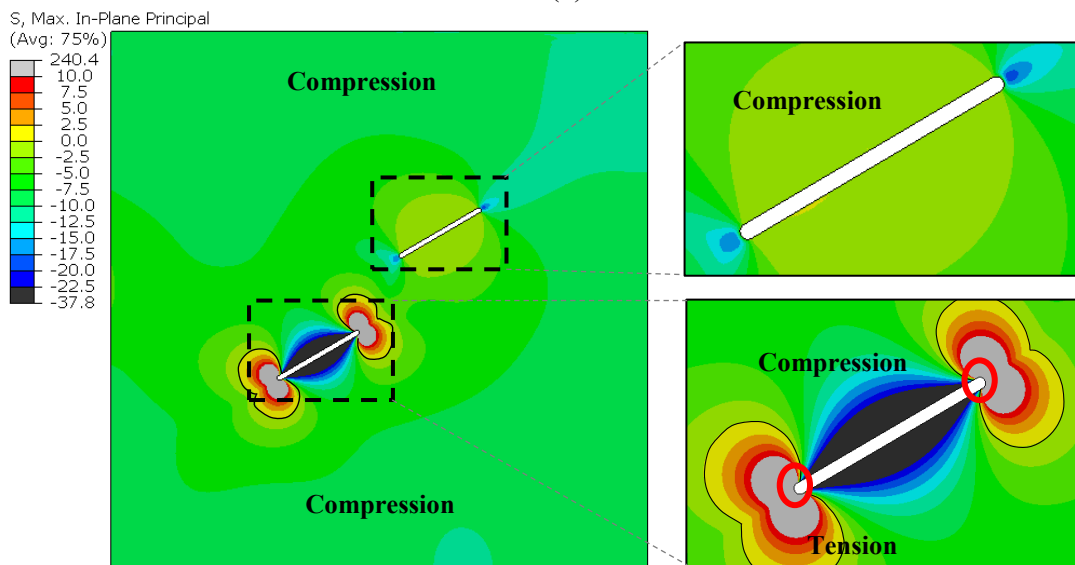
(b)



(c)



(d)



(e)

Fig. 9. Maximum principal stress contours under biaxial loading with circles showing the location of the highest tensile stress (a) Case 1 (b) Case 2 (c) Case 3 (d) Case 4 (e) Case 5.

Note: The same color scale was used in figures 8 and 9 to facilitate the interpretation of the variations of the stresses.

3.2. Stresses around the Flaw Tips

In this section of the paper, the variation of the maximum principal stresses (σ_1) and maximum shear stresses (τ_{\max}) are analyzed around the tips of the flaws following the paths shown in figure 5a. The uniaxial loading cases shown in table 2 are discussed in Subsection 3.2.1 and the biaxial loading cases shown in table 3 are discussed in Subsection 3.2.2. The loading cases defined previously are treated in this subsection as ratios between the hydraulic pressures applied inside the flaw and the vertical load, or HP/VL.

3.2.1 Uniaxial Loading Condition

Figures 10 and 11 show the variation of the maximum principal stresses around the inner tips of the pressurized and non-pressurized flaws, respectively. The dashed lines with arrows point the direction in which the maximum

principal stress changes with increasing HP/VL in the pressurized flaw. In the pressurized flaw, the highest tensile maximum principal stress for $HP/VL > 1.0$ is initially located near the upper face of the flaw (Point 1). The maximum principal stress at Point 1 decreases with increasing HP/VL and when $HP/VL > 1.0$, the highest tensile stress moves towards the center of the flaw tip (Points 4 to 7), which suggests that tensile cracks can initiate at this location when $HP/VL > 1.0$. The maximum principal stresses become more compressive towards the lower face of the tip (Points 9 to 11) with the increase in HP/VL. The non-pressurized flaw shown in figure 11 shows that the highest compressive stress occurs ahead of the tip (Point 5) and the highest tensile stress in the lower face of the flaw (Points 10/11). It can also be noticed that the maximum principal stresses are almost zero in the upper face of the flaw and that the compression observed from Points 4 to 6 tends to decrease as HP/VL increases.

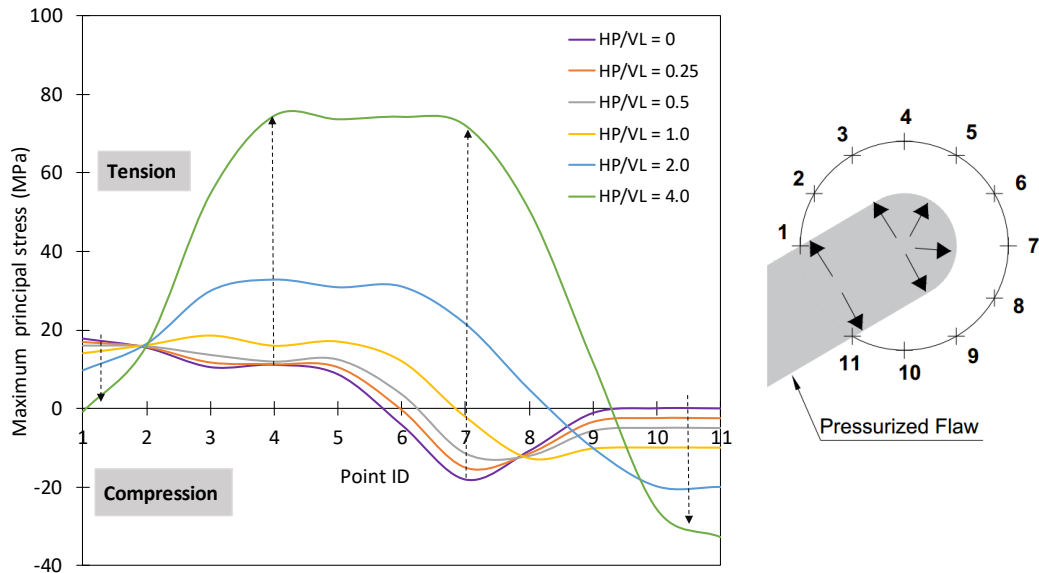


Fig. 10. Variation of the maximum principal stresses around the pressurized flaw tip for the uniaxial loading condition.

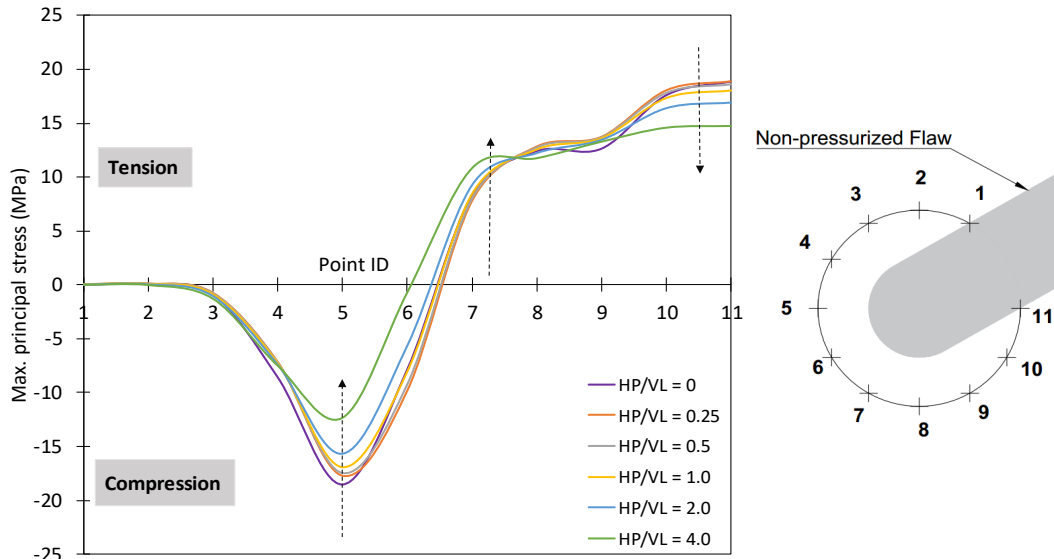


Fig. 11. Variation of the maximum principal stresses around the non-pressurized flaw tip for the uniaxial loading condition.

The maximum principal stresses are mainly tensile in the lower face of the non-pressurized flaw which suggests that tensile cracks may initiate from Points 8 to 11. However, the tension in the non-pressurized flaw is smaller in magnitude than in the pressurized flaw for most HP/VL, which suggests that a tensile crack will always initiate from the pressurized flaw, as intuitively expected.

Figures 12 and 13 show the variation of the maximum shear stresses under the uniaxial loading in the pressurized and non-pressurized flaws, respectively. In the pressurized flaw, it is difficult to interpret the variation of the maximum shear stress when HP/VL increases from 0 to 1.0. Once HP/VL is increased from 1.0 to 4.0 it is observed that the maximum shear stresses increase significantly (figure 12) with the highest maximum shear stresses located at Point 3 in the upper face of the tip and at Points 7 and 8 in the lower face of the tip. In the non-pressurized flaw (figure 13), it is clear that with the increase of HP/VL from 0 to 4.0, the maximum shear stresses decrease except for a minor increase at Point 1. This suggests that shear cracks cannot theoretically occur

at this flaw tip under this loading conditions as HP is increased.

3.2.2 Biaxial Loading Condition

Figures 14 and 15 show the variation of the maximum principal stresses under biaxial loading around the inner tips of the pressurized and non-pressurized flaws, respectively. From figure 14, one observes that the maximum principal stresses are initially in compression around the flaw tip until HP/VL=1.0. This is very different from the uniaxial case, in which significant tensile stresses occur for HP/VL ≤ 1.0. When HP/VL is increased from 2.0 to 4.0, the maximum principal stresses are mainly tensile from Points 4 to 8 with the highest tensile stress near Points 6 to 8 suggesting that tensile cracks might occur in this region. In the non-pressurized flaw tip, the maximum principal stresses are almost zero in the upper and lower faces of the tip (figure 15). Overall, the non-pressurized flaw is under compression, which decreases as HP/VL is increased. Hence, this suggests that tensile cracks may not initiate at the tip of the non-pressurized flaw.

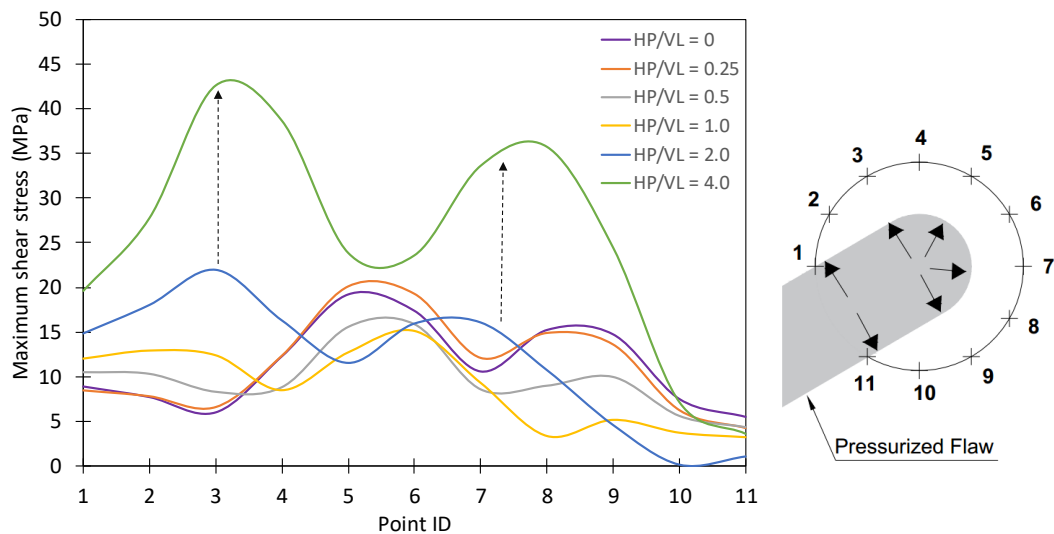


Fig. 12. Variation of the maximum shear stresses around the pressurized flaw tip for the uniaxial loading condition.

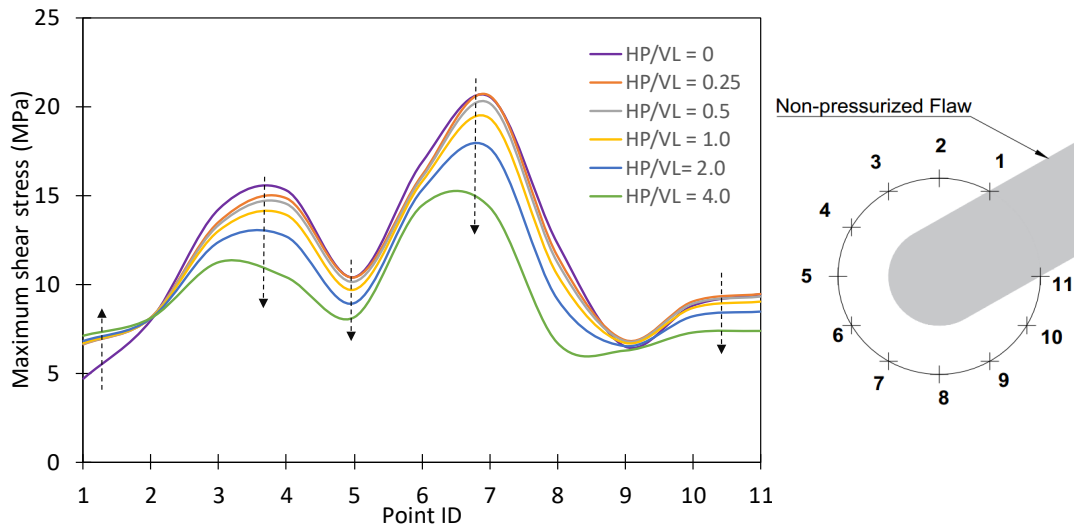


Fig. 13. Variation of the maximum shear stresses around the non-pressurized flaw tip for the uniaxial loading condition.

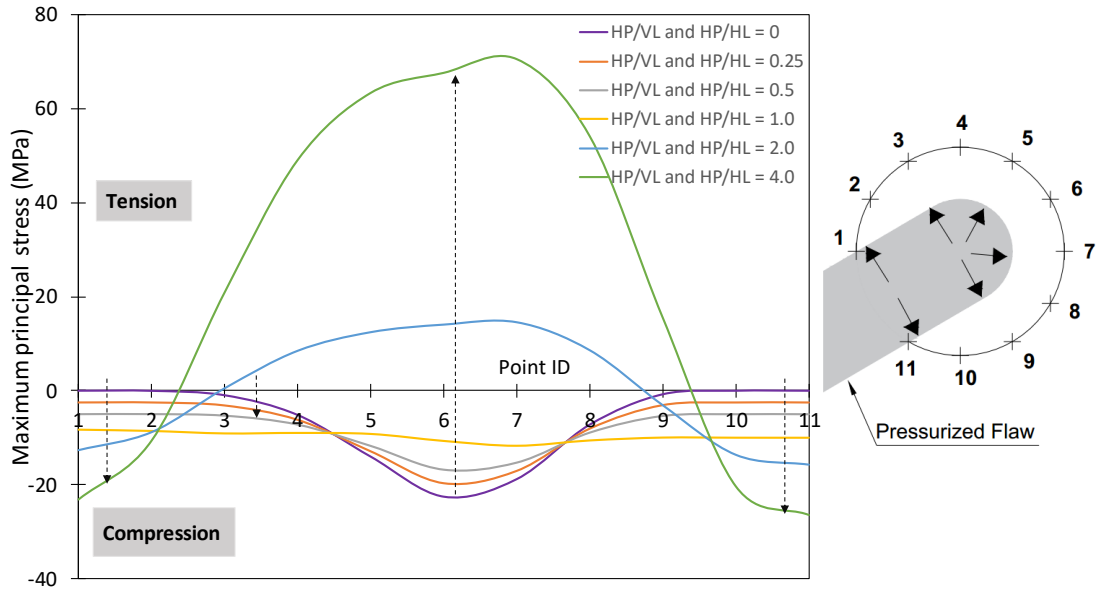


Fig. 14. Variation of the maximum principal stresses around the pressurized flaw tip for the biaxial loading condition.

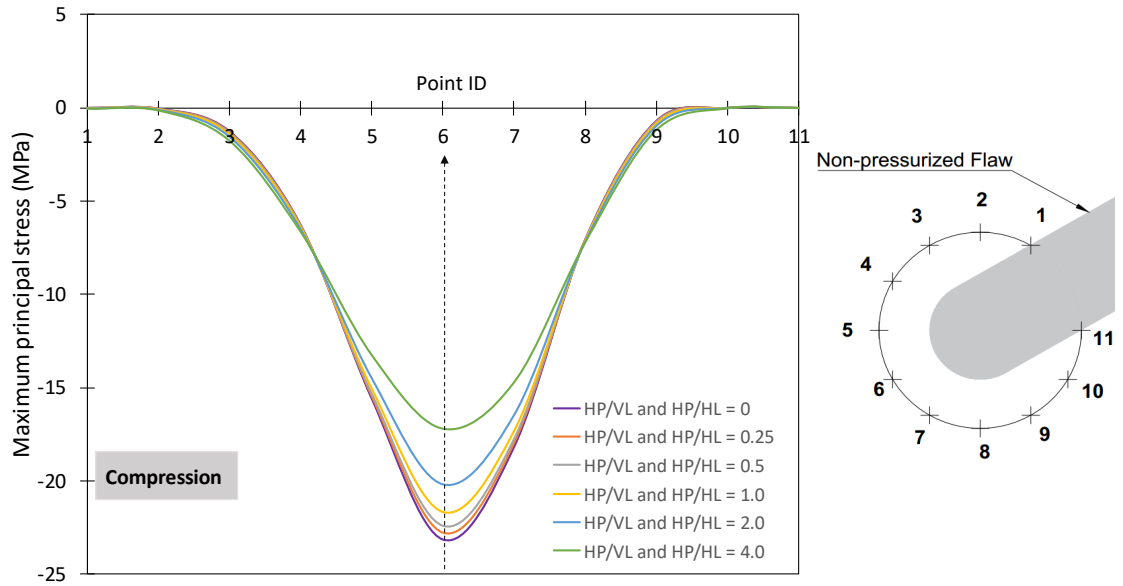


Fig. 15. Variation of the maximum principal stresses around the non-pressurized flaw tip for the biaxial loading condition.

Figures 16 and 17 show the variation of the maximum shear stresses under the biaxial loading in the pressurized and non-pressurized flaws, respectively. In the pressurized flaw, the maximum shear stresses decrease with the increase of HP/VL from 0 to 1.0. When HP/VL is increased from 2.0 to 4.0, the maximum shear stresses increase significantly (figure 16) with the highest maximum shear stress occurring near Point 4 in the upper face of the tip and Point 8 in the lower face of the tip.

As previously observed for the uniaxial loading condition and non-pressurized flaw it is clear that, with the increase of HP/VL from 0 to 4.0, the maximum shear stresses decrease overall (except for a minor increase at Point 11). This suggests that shear cracks cannot theoretically occur in this flaw tip under this loading conditions as HP is increased.

3.3. Stresses in the Bridge between Inner Flaw Tips

In this section of the paper, the variation of maximum principal stresses (σ) and maximum shear stresses (τ_{\max}) are analyzed along the path shown in figure 5b. The uniaxial loading cases shown in table 2 are discussed in Subsection 3.3.1 and the biaxial loading cases shown in table 3 are discussed in Subsection 3.3.2.

3.3.1 Uniaxial Loading Condition

Figure 18 shows that the maximum principal stresses are mainly tensile under uniaxial loading in the bridge region. It is also clear that the maximum principal stresses tend to increase with increasing HP/VL ratios, as intuitively expected.

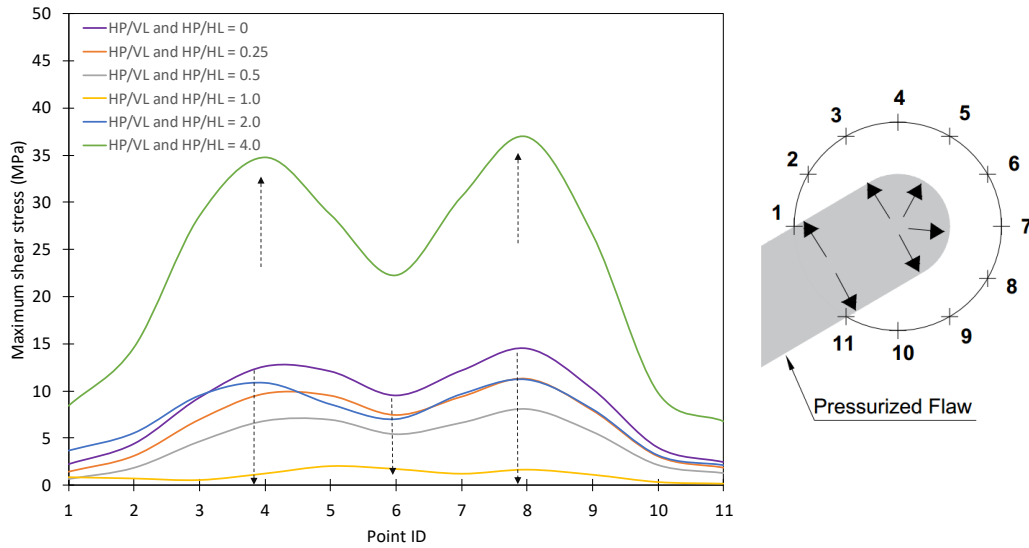


Fig. 16. Variation of the maximum shear stresses around the pressurized flaw tip for the biaxial loading condition.

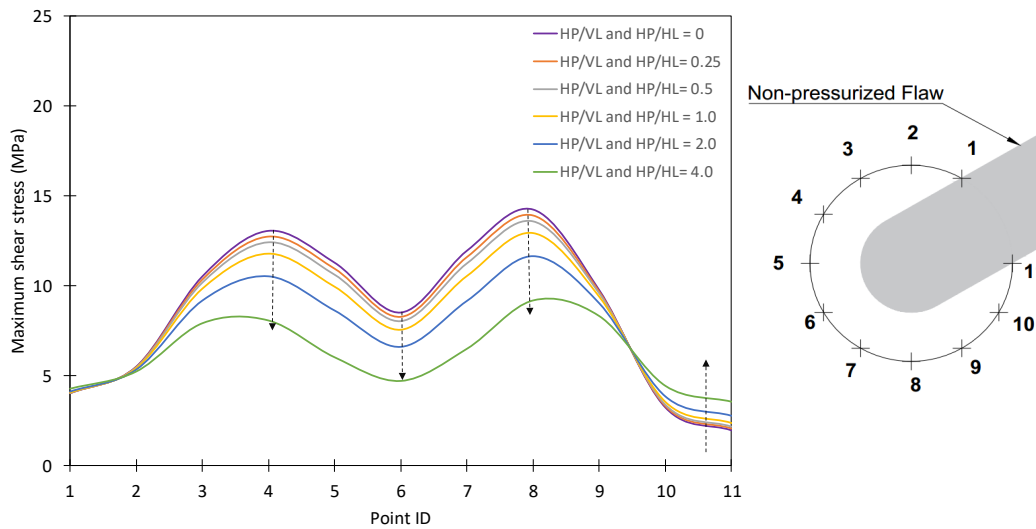


Fig. 17. Variation of the maximum shear stresses around the non-pressurized flaw tip for the biaxial loading condition.

In figure 19, it is observed that the maximum shear stresses decrease from $HP/VL=0$ to 1.0 near the pressurized flaw tip (Point 1) and increase for $HP/VL>1.0$. Hence, while it is unlikely that shear cracks can occur when $HP/VL\leq 1.0$ near the tip of the pressurized flaw, they may initiate when $HP/VL>1.0$. On the other hand, near the non-pressurized flaw tip (Point 10), the maximum shear stress decreases as HP/VL is increased, which indicates that no shear crack may theoretically initiate at this location as HP/VL is increased.

In order to better interpret the results, Mohr stress circles are drawn for Points 1, 5 and 10 along the path connecting the two flaws under each loading case (figure 20). By doing this, one can not only analyze the variation of the maximum principal stresses (σ_I), but also the minimum principal stresses (σ_{II}) and the maximum shear stresses (σ_{max}) simultaneously on the same plot. For Point 1 in figure 20a, it is interesting to observe that for $HP/VL\leq 1.0$, the minimum principal stresses are always

compressive, and the maximum shear stresses (radii of the Mohr circles) decrease as HP/VL is increased. When $HP/VL>1$, both principal stresses are tensile, which can facilitate the initiation of tensile cracks, and the maximum shear stresses increase substantially as HP/VL increases, which may also cause the initiation of shear cracks. For Point 5, it is observed that the minimum principal stress is always negative, while the maximum principal stress is always tensile but only increases slightly as HP/VL is increased. These observations suggest that tensile cracks may not occur in the bridge between flaw tips. Similarly, shear cracks are unlikely to occur, since the maximum shear stress progressively decreases as HP/VL is increased. Most of the observations made for Point 5 are also valid for Point 10. The main differences are that tensile maximum principal stresses are only observed for $HP/VL>1.0$, and that the absolute values of the maximum shear stresses are always higher than at Point 5.

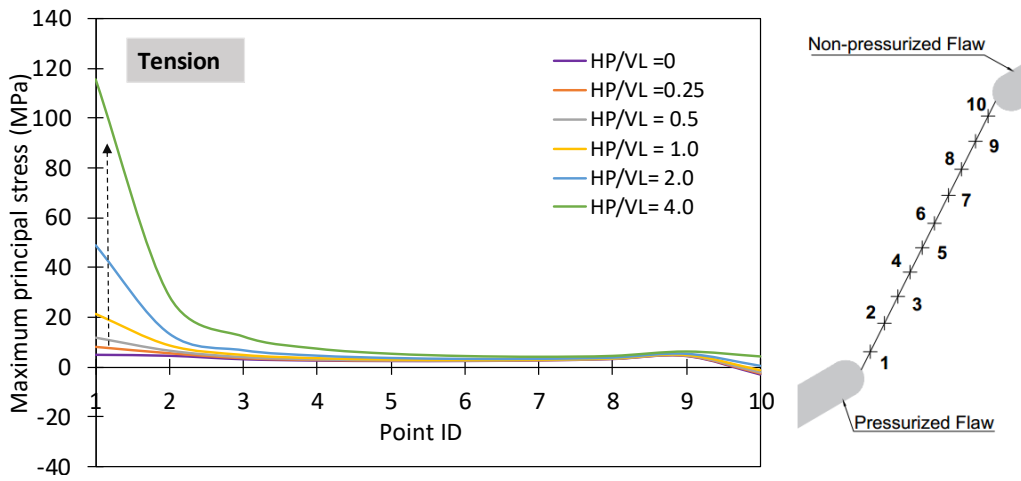


Fig. 18. Variation of the maximum principal stresses in the bridge region for the uniaxial loading condition.

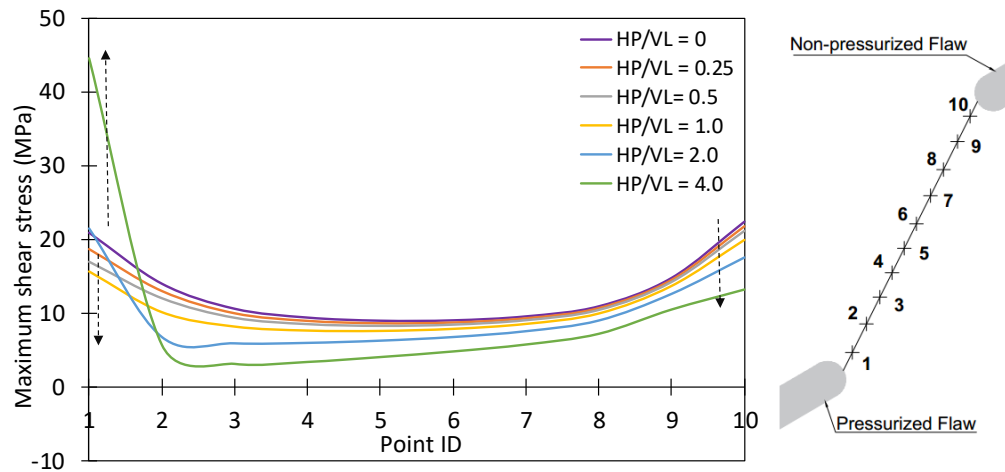


Fig. 19. Variation of the maximum shear stresses in the bridge region for the uniaxial loading condition.

3.3.2 Biaxial Loading Condition

Figure 21 shows that the maximum principal stresses in the bridge region are always compressive when $HP/VL \leq 1.0$. For $HP/VL > 1.0$ the maximum principal stresses become highly tensile but only near the pressurized flaw tip (Points 1 to 3). Hence, for the biaxial loading, tensile cracks may only occur near the pressurized tip when $HP/VL > 1.0$. Figure 22 shows the variation of the maximum shear stresses in the bridge region. It can be observed that near the pressurized flaw (Points 1 to 3), the maximum shear stresses decrease as HP/VL increase when $HP/VL \leq 1.0$ and increase when $HP/VL > 1.0$. Hence, it is unlikely that shear cracks occur when $HP/VL \leq 1.0$ but only when $HP/VL > 1.0$ near the tip of the pressurized flaw. On the other hand, near the non-pressurized flaw, the maximum shear stresses decrease as HP/VL increases. This behavior is identical to what was observed under uniaxial loading.

Similar to what was done for the uniaxial loading, Mohr stress circles were drawn for Points 1, 5 and 10 along the path connecting the two flaws under each loading case (figure 23). In figure 23a for Point 1, it is clear that both minimum and maximum principal stresses are

compressive for $HP/VL \leq 1.0$. When $HP/VL > 1.0$, the maximum principal stresses increase considerably, and both principal stresses become tensile for $HP/VL = 4.0$, thus tensile cracks can be initiated at Point 1 for high HP/VL . The maximum shear stresses decrease significantly as HP/VL increases from 0 to 1.0. When HP/VL increases from 1.0 to 4.0, the maximum shear stresses increase considerably. As such, it is possible that shear cracks may initiate from Point 1. For Point 5 (figure 23b), it is interesting to notice that both principal stresses are always compressive. The maximum shear stresses decrease as HP/VL increase from 0 to 2.0 and increase when HP/VL increases from 2.0 to 4.0. However, the absolute values of the maximum shear stresses are significantly lower than what is observed at Point 1. Hence, considering both facts, neither tensile nor shear cracks may theoretically initiate in the bridge between the two flaws. As similarly observed for Point 5, both principal stresses are compressive at Point 10. However, unlike Point 5, the maximum principal stresses only increase slightly when HP/VL increases from 0 to 4.0 and the maximum shear stresses gradually decrease as HP/VL increases from 0 to 4.0 at Point 10. As such, neither tensile nor shear cracks may theoretically initiate from Point 10.

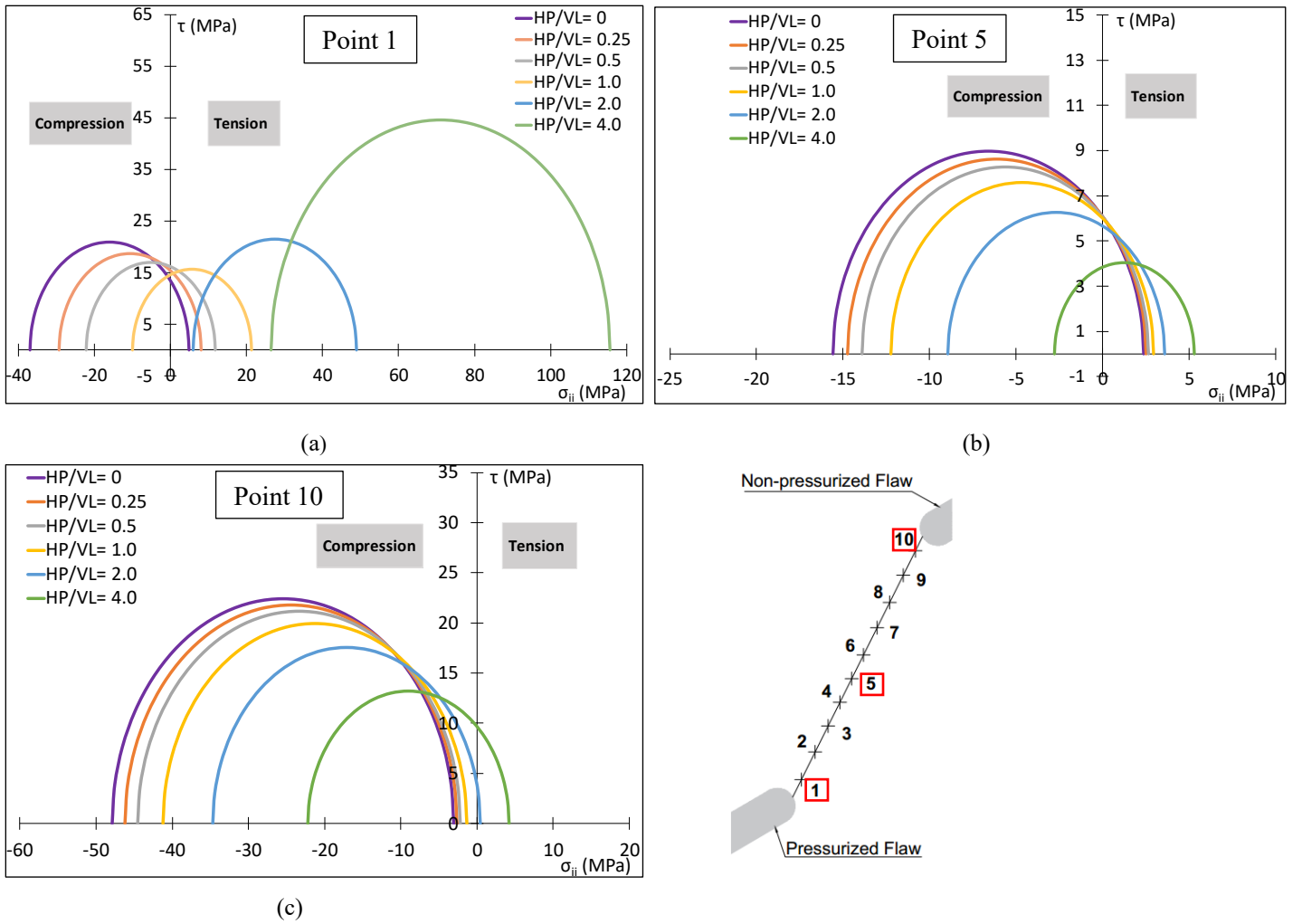


Fig.20. Mohr circles representing the variation of the state of stress under uniaxial loading in the bridge region at (a) Point 1, (b) Point 5, (c) Point 10.

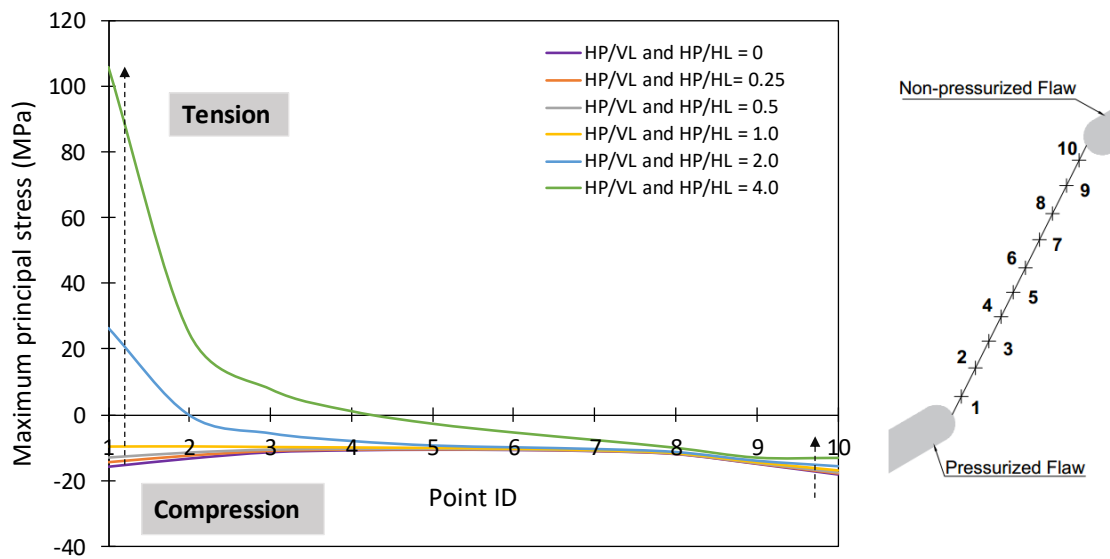


Fig. 21. Variation of the maximum principal stresses in the bridge region for the biaxial loading condition.

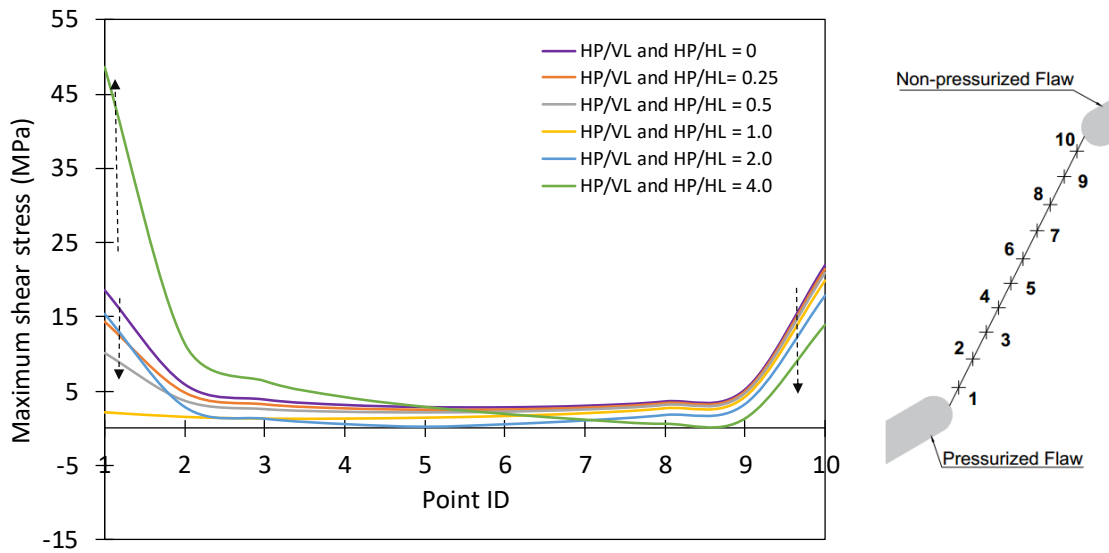


Fig. 22. Variation of the maximum principal stresses in the bridge region for the biaxial loading condition.

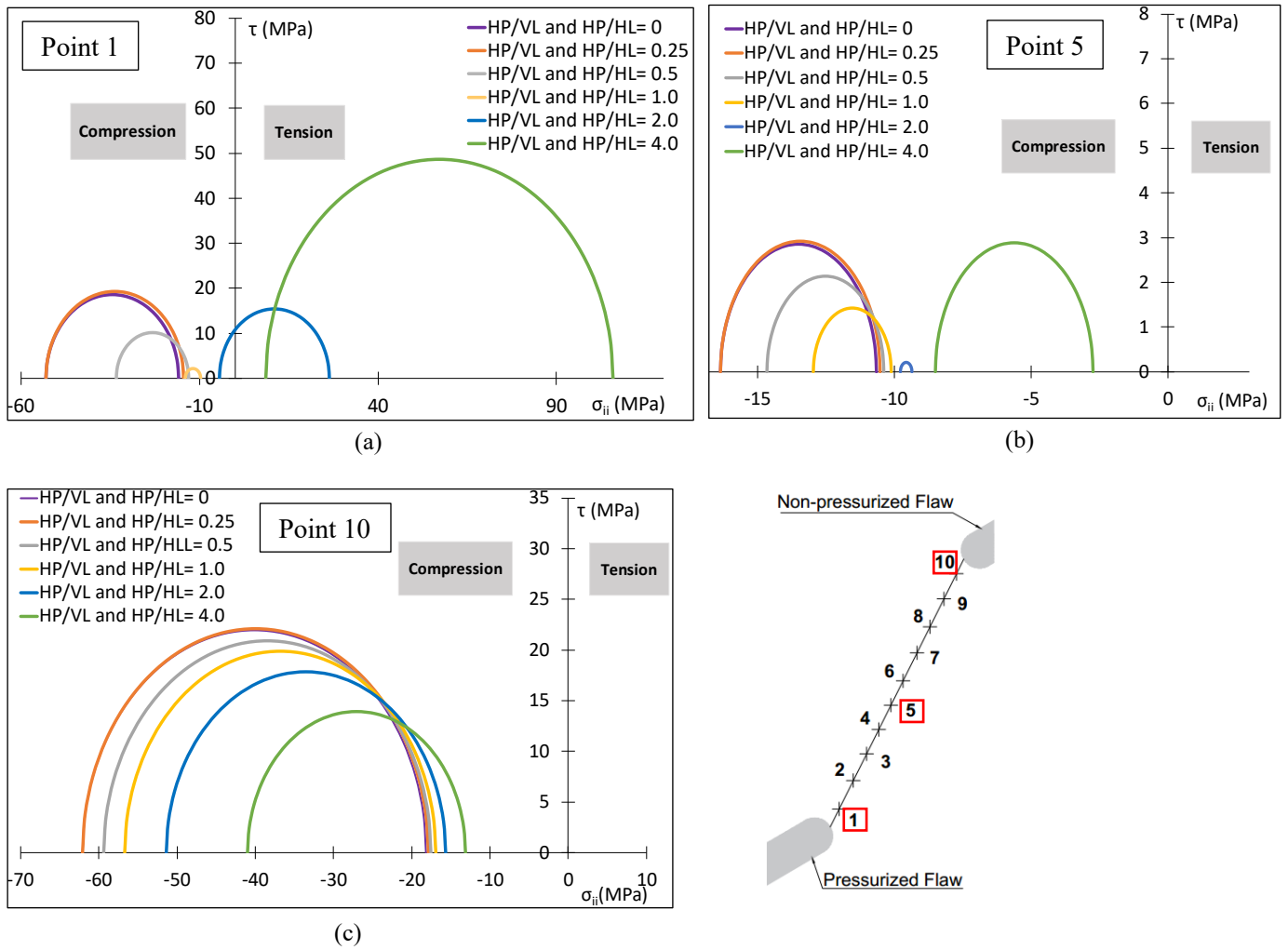


Fig.23. Mohr circles representing the variation of the state of stress under biaxial loading in the bridge region at (a) Point 1, (b) Point 5, (c) Point 10.

4. SUMMARY AND CONCLUSIONS

This numerical study investigated the variation of the stress field around two pre-fabricated flaws when only one is hydraulically pressurized and the specimen is subjected to either uniaxial or biaxial loading conditions. The maximum principal stresses and maximum shear stresses were evaluated in a large region accounting for both flaws, along a circular path around the flaw tips and along the bridge region connecting the inner tips of the pressurized and the non-pressurized flaws. In general, it is observed that important tensile stresses occur for the uniaxial condition for most cases analyzed; on the other hand, it is observed that the magnitude and the area under maximum principal compressive stresses are significantly larger than under maximum principal tensile stresses for the biaxial loading condition for all loading cases studied.

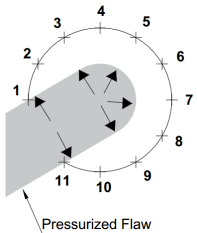
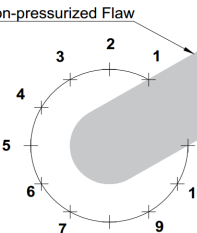
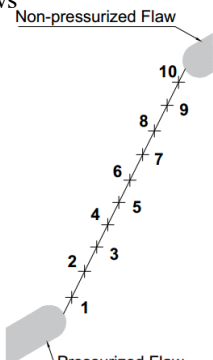
In order to relate the analyzed stress fields to possible crack initiation, it was considered that tensile and shear cracks may initiate from the locations where the maximum tensile principal stresses and maximum shear stresses, respectively, were the highest. Table 3 summarizes the most important observations related to crack initiation obtained in this paper.

The observations of this study are important to better understand the development of hydraulic fractures due to the interaction between pressurized and non-pressurized flaws. They will also be the theoretical basis for laboratory experiments that the authors' research group is designing and will soon be conducting.

5. ACKNOWLEDGEMENTS

The authors would like to express their gratitude for the support from NSF, through award number 1738081, under which the present study was conducted.

Table 3. Summary of the results obtained from the present numerical study

Location	Uniaxial Loading Condition	Bi-axial Loading Condition
<p>Pressurized flaw</p> 	<ul style="list-style-type: none"> Tensile cracks can initiate when $HP/VL > 1.0$ at Points 4/5. No significant variation of the maximum shear stress is observed for $HP/VL \leq 1.0$. Shear cracks can occur near Points 3, 7-8 of the pressurized flaw when $HP/VL > 1.0$. 	<ul style="list-style-type: none"> Maximum principal stresses are compressive when $HP/VL \leq 1.0$. When $HP/VL > 1.0$, maximum principal stresses are tensile ahead of the tip. Tensile cracks can initiate from Point 4 to 8 where the highest tensile stress occur. For $HP/VL > 1.0$, the maximum shear stresses increase significantly. The highest maximum shear stress occurring near Points 4 and 8 where shear cracks may occur.
<p>Non-pressurized flaw</p> 	<ul style="list-style-type: none"> Tension in non-pressurized flaw is smaller than in the pressurized flaw for most HP/VL. Tensile crack will always initiate in the pressurized flaw. When HP/VL increases from 0 to 4.0, the maximum shear stresses decrease in general. Shear cracks cannot occur in this flaw tip under this loading conditions as HP is increased. 	<ul style="list-style-type: none"> Overall, the non-pressurized flaw is under compression. Moreover, the maximum shear stresses decrease as HP/VL increases. Neither tensile nor shear cracks may initiate at the tips of the non-pressurized flaw.
<p>Bridge between two flaws</p> 	<ul style="list-style-type: none"> Maximum principal stresses are mainly tensile. When $HP/VL > 1.0$, tensile cracks can initiate from the tip of pressurized flaw. Neither tensile nor shear cracks are likely to initiate in the bridge region as HP/VL is increased. 	<ul style="list-style-type: none"> Both tensile and shear cracks may occur near the pressurized tip when $HP/VL > 1.0$. Neither tensile nor shear cracks may initiate in the bridge between the two flaws as HP/VL is increased.

REFERENCES

- AlDajani, O. A. (2017). *Fracture and Hydraulic Fracture Initiation, Propagation and Coalescence in Shale (Ph.D Thesis)*. Massachusetts Institute of Technology.
- Bobet, A. (1997). *Fracture Coalescence in Rock Materials: Experimental Observations and Numerical Predictions (Ph.D Thesis)*. Massachusetts Institute of Technology.
- Carpinteri, A. (1991). Size-scale transition from ductile to brittle failure: structural response vs. crack growth resistance curve. *International Journal of Fracture*, 51(2), 175–186. <https://doi.org/10.1007/BF00033977>
- Chan, M. (1986). *Automatic two-dimensional multi-fracture propagation modelling of brittle solids with particular application to rock (Ph.D Thesis)*. Massachusetts Institute of Technology.
- Chan, M., Li, V., & Einstein, H. H. (1990). A hybridized displacement discontinuity and indirect boundary element method to model fracture propagation. *International Journal of Fracture*, 45(4), 263–282. <https://doi.org/10.1007/BF00036271>
- Gonçalves da Silva, B., & Einstein, H. H. (2014). Finite Element study of fracture initiation in flaws subject to internal fluid pressure and vertical stress. *International Journal of Solids and Structures*, 51(23–24), 4122–4136. <https://doi.org/10.1016/J.IJSOLSTR.2014.08.006>
- Gonçalves da Silva, B. G. (2016). *Fracturing processes and induced seismicity due to the hydraulic fracturing of rocks (Ph.D Thesis)*. Massachusetts Institute of Technology.
- Gordeliy, E., & Detournay, E. (2011). Displacement discontinuity method for modeling axisymmetric cracks in an elastic half-space. *International Journal of Solids and Structures*, 48(19), 2614–2629. <https://doi.org/10.1016/J.IJSOLSTR.2011.05.009>
- Lajtai, E. Z. (1971). A theoretical and experimental evaluation of the Griffith theory of brittle fracture. *Tectonophysics*, 11(2), 129–156. [https://doi.org/10.1016/0040-1951\(71\)90060-6](https://doi.org/10.1016/0040-1951(71)90060-6)
- Liu, Y. (2016). On the displacement discontinuity method and the boundary element method for solving 3-D crack problems. *Engineering Fracture Mechanics*, 164, 35–45. <https://doi.org/10.1016/J.ENGFRACMECH.2016.07.009>
- Miller, J. . (2008). *Crack coalescence in Granite (MS.c Thesis)*. Massachusetts Institute of Technology.
- Potyondy, D. O., & Cundall, P. A. (2004). A bonded-particle model for rock. *International Journal of Rock Mechanics and Mining Sciences*, 41(8), 1329–1364. <https://doi.org/10.1016/J.IJRMMS.2004.09.011>
- Rice, J. R. (1968). A Path Independent Integral and the Approximate Analysis of Strain Concentration by Notches and Cracks. *Journal of Applied Mechanics*, 35(2), 379–386. Retrieved from <http://dx.doi.org/10.1115/1.3601206>
- Vasarhelyi, B., & Bobet, A. (2000). Modeling of Crack Initiation, Propagation and Coalescence in Uniaxial Compression. *Rock Mechanics and Rock Engineering*, 33, 119–139. <https://doi.org/10.1007/s006030050038>
- Wong, L. N. Y. (2008). *Crack Coalescence in Molded Gypsum and Carrara Marble (Ph.D Thesis)*. Massachusetts Institute of Technology.
- Yang, S. Q., Jiang, Y. Z., Xu, W. Y., & Chen, X. Q. (2008). Experimental investigation on strength and failure behavior of pre-cracked marble under conventional triaxial compression. *International Journal of Solids and Structures*, 45(17), 4796–4819. <https://doi.org/10.1016/j.ijsolstr.2008.04.023>
- Yu, T. T. (2011). The extended finite element method (XFEM) for discontinuous rock masses. *Engineering Computations*, 28(3), 340–369. <https://doi.org/10.1108/02644401111118178>